IOP Publishing Classical and Quantum Gravity

Class. Quantum Grav. 36 (2019) 075007 (20pp) https://doi.org/10.1088/1361-6382/ab075e

A multistage vibration isolation system for Advanced Virgo suspended optical benches

J V van Heijningen[1,2,3], A Bertolini[1], E Hennes[1], M G Beker[1,2,4], M Doets[1], H J Bulten[1,2], K Agatsuma[1,5], T Sekiguchi[6] and J F J van den Brand[1,2]

[1] National Institute for Subatomic Physics Nikhef, Science Park 105, 1098 XG Amsterdam, The Netherlands
[2] VU University, De Boelelaan 1105, 1081 HV Amsterdam, The Netherlands

E-mail: joris.vanheijningen@uwa.edu.au

Received 19 November 2018, revised 6 January 2019
Accepted for publication 15 February 2019
Published 11 March 2019

Abstract

We present a compact, vacuum compatible seismic attenuation system designed to isolate five auxiliary optical benches for Advanced Virgo, a second generation gravitational wave detector. We report on the design of the device, coined MultiSAS (multistage seismic attenuation system) and on its measured vibration isolation performance. The latter can be summarized by quoting a payload isolation ratio at 10 Hz of 100 dB and 140 dB in vertical and horizontal, respectively. We also present the design and performance of the MultiSAS control system along the translation degrees of freedom, as well as a discussion of the possible coupling to the angular degrees of freedom. Over a time-scale of 100 s, 1 μm magnitude RMS for translational degrees of freedom is achieved for seismic conditions observed in the past five years at the Virgo site and in Amsterdam. The spectral displacement levels are expected to be lower than 10^{-14} m $\text{Hz}^{-1/2}$ from 10 Hz onwards in vertical and horizontal. In addition we discuss effects that could deteriorate the performance of the device such as thermal drifts of the mechanical filters, residual acoustic coupling and cradle effects on the inverted pendulum pre-isolation stage. Mitigation strategies or solutions were devised and installed in the five Advanced Virgo systems.

[3] Present affiliation: OzGrav-UWA node, University of Western Australia, 35 Stirling Hwy, Crawley WA 6009, Australia
[4] Present affiliation: Innoseis B.V., Science Park 105, 1098 XG Amsterdam, The Netherlands
[5] Present affiliation: The University of Birmingham, Edgbaston, Birmingham B15 2TT, United Kingdom
[6] Present affiliation: Halley Valley Co. Ltd., Taiyo-Life Shinagawa Building 28F, 2-16-2 Konan, Minato-ku, Tokyo 108-0075, Japan

Keywords: gravitational waves, vibration isolation, seismic noise, controls

(Some figures may appear in colour only in the online journal)

1. Introduction

With the detection of gravitational waves (GWs) [1], mankind has made its most precise distance measurement to date. After Advanced Virgo [2] joined the global GW detector network, the first triple-coincident measurement of GWs measured by Advanced Virgo and the two LIGO detectors [3], GW170814, was made in August 2017 [4]. Three days after Advanced Virgo's first detection, the first coincidental measurement of GWs with electromagnetic counterparts, GW170817, from a binary neutron star merger [5, 6] has provided a firm basis for the newly founded field of multi-messenger gravitational wave astronomy.

The detections would not have been achievable without the vibration isolation of all components of the gravitational wave detectors. In line with the earlier vibration isolation strategy of initial Virgo [7], all new seismic attenuation systems for auxiliary optical benches for Advanced Virgo achieve their (in-band) performance through passive isolation by suspension of the optical benches. Active feedback is only used to control the low-frequency rigid body modes of the isolation chain. The vibration isolation system of Advanced Virgo core components, i.e. the *superattenuators* [8], remained essentially as what was used in initial Virgo.

Scattered light is modulated by the residual seismic motion of the bench. The non-linear behavior of this coupling leads to the upconversion of low-frequency seismic excitations ($<$10 Hz) into the detection band ($>$10 Hz) [9, 10]. This was a serious limitation on the achievable sensitivity of first generation detectors including Initial Virgo [11]. In Advanced Virgo, the benches housing auxiliary optics generating error signals to control the interferometer are suspended and in vacuum. This choice was made to limit the vibrations of the optical sensors themselves that can couple to the alignment control signals [12], and to mitigate the noise caused by the light scattered back towards the interferometer by the control photodiodes and their telescope optics. Any bench motion will be indistinguishable from a beam displacement on the suspended auxiliary optics due to a misalignment of the cavity mirrors. Hence the real bench displacement noise should not exceed the optical sensor shot noise contribution to the measurement.

Development of new multistage systems dedicated to several other components was necessary, which we report on here. We base our design on earlier seismic attenuation work [13–15], in particular [16]. Five of these isolation stages, called MultiSAS, are part of the Advanced Virgo design, as shown in figure 1. The photodiodes responsible for measuring the GW signal of GW170814 and GW170817 are positioned on an optical bench suspended by MultiSAS.

In section 2 we summarize the extensive characterization campaign of the MultiSAS prototype, including an overview of lessons learned and improvements implemented in the final design of the five Advanced Virgo systems. The results and performance of the MultiSAS prototype are presented in section 3. In section 4, various performance deteriorating issues and their solution/mitigation strategies are discussed. The dynamics of the system is sensed and a dedicated control system has been developed to damp mechanical modes and to control the position of the suspended objects, e.g. optical benches, in 6 degrees of freedom, which is presented in section 5. Finally, we make concluding remarks and discuss future work towards next generation gravitational wave detectors.

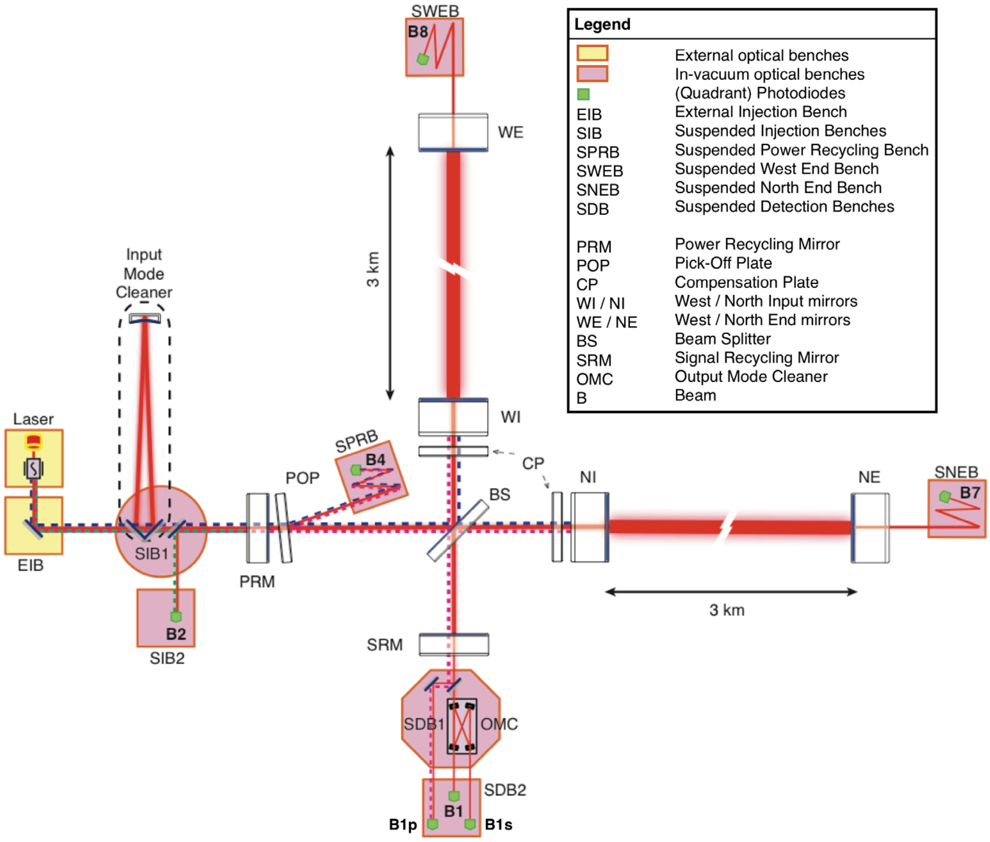

Figure 1. The optical set-up for Advanced Virgo showing the interferometer with 3 km long Fabry Perot cavities and a selection of the major optical benches. Various (quadrant) photodiodes, housed on optical benches suspended by MultiSAS indicated by the five pink squares, generate control signals for interferometer control. Dashed lines indicate modulated light used for locking the different cavities. Several beams important to interferometer locking and detection are denoted by 'B' followed by a number. Figure adapted with permission from [17].

2. MultiSAS design

MultiSAS is designed to comply with requirements set by optical simulations for the auxiliary optics of Advanced Virgo. All auxiliary optical bench motion is to be such that there is no impact on the Advanced Virgo, observing a safety factor of 10. The seismic attenuation system aims to meet RMS requirements as well as amplitude spectral density (ASD) requirements for the bench motion at 10 Hz. A summary of the requirements is given in table 1.

The system aims to meet these requirements by using chains of low natural frequency ($f_0 < 1$ Hz) mechanical filters. The mechanical filters are an inverted pendulum and two simple pendulums for horizontal isolation and two cascaded geometric anti-spring (GAS) [18] filters for vertical isolation. A multistage system adopting GAS filters and a pendulum pre-isolator, has been developed for the KAGRA detector [19]. The core development of GAS multi-stage vibration isolation system and the design methods, leading to the successful implementation, are explained in this paper. Figure 2 shows the complete mechanical design of MultiSAS.

Table 1. Requirements [12] for the three translational and three angular degrees of freedom of the optical benches suspended by MultiSAS.

	Translational	Angular
Integrated RMS (down to 10 mHz)	1.0×10^{-6} m	3.1×10^{-8} rad
ASD from 10 Hz onwards	2.1×10^{-12} m Hz$^{-1/2}$	3.3×10^{-15} rad Hz$^{-1/2}$

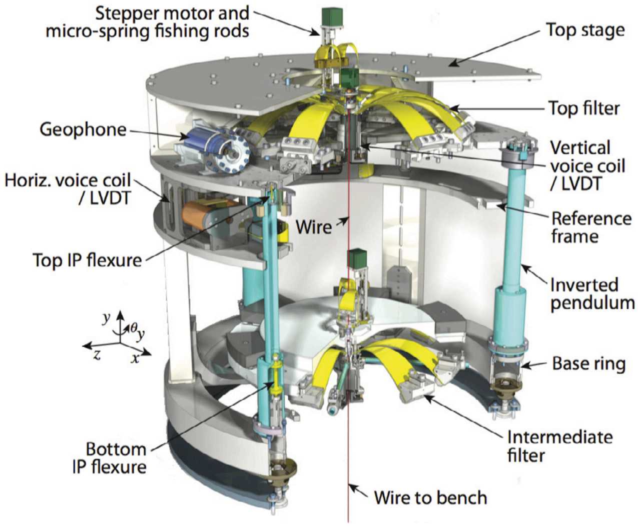

Figure 2. Overview of the MultiSAS isolation system. The inverted pendulum stage is shown in turquoise and the GAS filters are shown in yellow. Between the GAS filters, the wires acting as pendulums are shown in red. The position of sensors (geophones and LVDTs) and actuators (voice coils) are visible in the structure. The top and intermediate filters have stepper motors with thin blade springs or *fishing rods* for vertical positioning. The Virgo coordinate system is displayed, which will be used throughout this paper. It has the z-direction along the beam and the y-direction as vertical.

Each system is placed in a *MiniTower* and the base ring rests on a support inside this vacuum vessel, as is shown in figure 3. From the base ring, the inverted pendulum stage supports the top stage. From the first GAS filter stage, a wire suspends the intermediate filter. The intermediate filter body holds a second set of GAS blade springs, which suspends the optical bench via another wire. The two wires provide compliance as the intermediate filter and benches act as pendulum masses, providing two more stages of horizontal isolation in the form of a double pendulum. The whole system fits in one cubic meter to be compliant with the limited space available in the existing Virgo infrastructure.

The fishing rod (see figure 2) is a set of beryllium copper thin blade springs on a base that moves vertically on a stepper motor. This results in a variable DC vertical pulling force that can be altered when for example a temperature change affects the vertical position of the GAS filters.

In a GAS filter, the blades are held in place by clamps on the outside, while their tips are connected to a single *keystone* from which the intermediate stage or payload is suspended. This keystone is designed to move in the vertical degree of freedom and to be geometrically

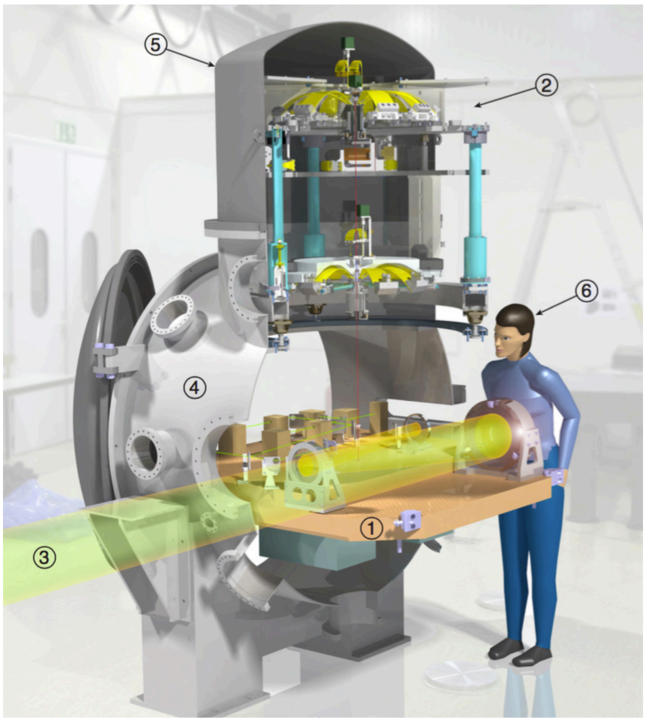

Figure 3. An impression of MultiSAS suspending an Advanced Virgo optical (end) bench in a MiniTower vacuum chamber. (1) Optical bench. (2) MultiSAS. (3) Transmission beam from end mirror. (4) MiniTower vacuum chamber. (5) Removable cupola. (6) Observant physicist.

stiff in all other degrees of freedom. High frequency (>50 Hz) modes in translational and angular keystone modes exist and these are discussed at the end of next section.

A set of sensors and actuators is used to effectively damp the rigid body modes of the system, without spoiling the passive isolation performance. Bench translational control, to be discussed in section 5, uses sensors, i.e. LVDTs [20] and geophones, and actuators, i.e. voice coils, at the top stage. Vertical control is done only with the top filter LVDT/voice coil pair.

3. Isolation performance

The inverted pendulum stage and GAS filters were individually tested. The transfer function of the inverted pendulum stage was determined by loading it with a dummy mass from a single pendulum (see figure 4(a)).The primary motivation for the measurement was to tune the center of percussion effect [16] by adjusting the counterweights at the bottom of the inverted pendulum legs.

The inverted pendulum stage was put on a shaker stage driven by piezoelectric actuators (see figure 4(b)) to measure the horizontal transfer function. In order to measure a transfer function, horizontal accelerometers were placed on the base ring as well as the top stage. We tuned the center of percussion effect by adding or removing mass from the *counterweight holding bell* located at the bottom of the inverted pendulum legs (see figure 2, below the *bottom IP flexure*). It was determined that five blocks of 140 g, totalling 700 g per inverted

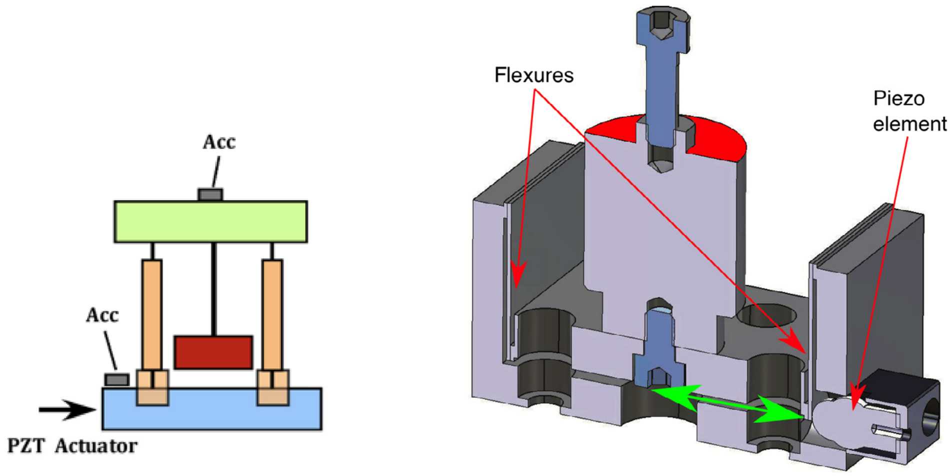

(a) (b)

Figure 4. Panel (a) shows a cartoon of the set-up for the inverted pendulum stage transfer function measurement. Horizontal accelerometers are used to record the transfer function. To avoid exciting the reference frame modes, the reference frame was detached and lifted from the base ring. Tilt coupling to the top stage accelerometer proved to be a problem and much effort was put in positioning it to mitigate these issues. Panel (b) shows a CAD drawing of a piezo shaker. The base ring rests on three custom made horizontal flexure stages driven by piezo actuators. The green arrow indicates the direction of motion.

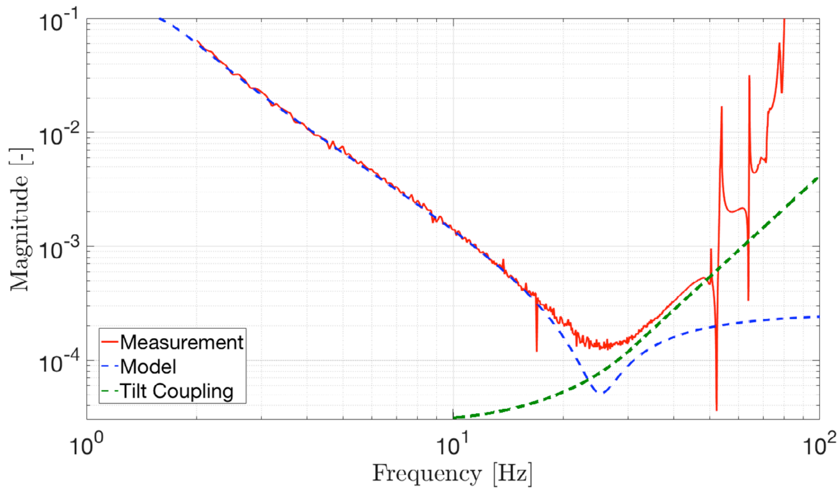

Figure 5. Inverted pendulum transfer function measurement result. The center of percussion effect is modeled to be slightly overcompensated with a $Q = 5$ resonant zero at 25 Hz. The saturation level is almost 80 dB. Residual tilt coupling of the measurement set-up is visible from 25 Hz onwards. This is a roll-up of a tilt resonance of the piezo suspension shown in figure 4(b) and a measurement artifact. Several internal modes of the shaker stage are visible above 50 Hz.

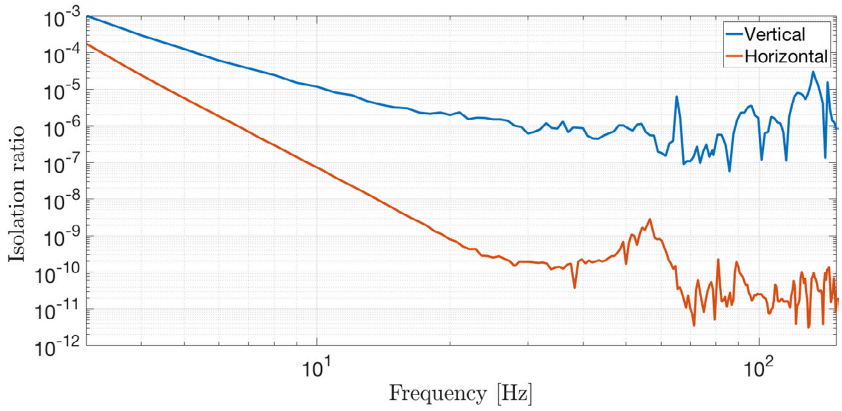

Figure 6. Vertical [17] and horizontal transfer functions of MultiSAS. Both results are obtained by multiplying intermediate transfer functions, e.g. from actuator structure to top stage to characterize the inverted pendulum stage. The structures from 65 Hz onwards in vertical are resonances of modes of the system, where the first higher order vertical mode at 135 Hz is associated with an intermediate filter keystone bouncing mode. The structure from 40 Hz onwards in horizontal are the (damped) keystone modes described below.

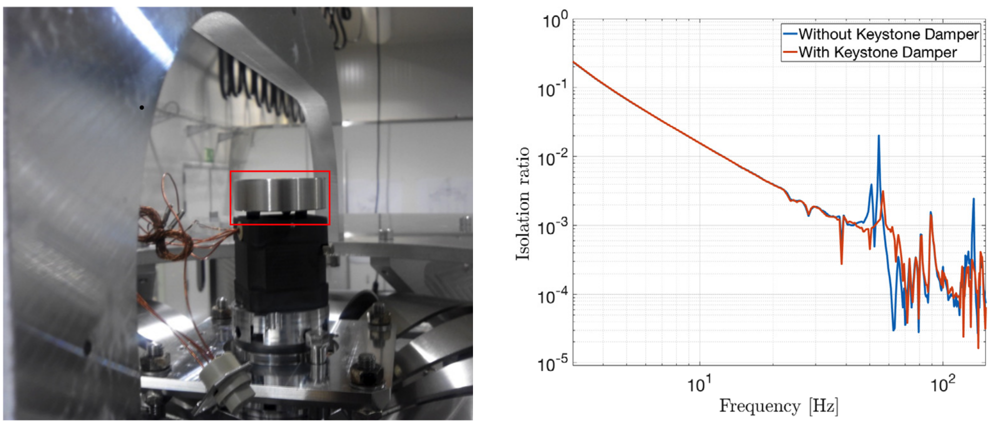

(a) (b)

Figure 7. Effect of a damper on the MultiSAS Topstage GAS filter keystone: (a) a photograph of the damper (a mass on viton spheres, see red rectangle) on the stepper motor near the topstage keystone and (b) a comparison in horizontal isolation ratio from top stage to intermediate filter without and with such a damper. The keystone resonances are the peaks at 55 Hz and 125 Hz. Other structures found at 80 Hz, between 75 Hz and 100 Hz and between 140 Hz and 150 Hz are the resonance of the filter frame, coupling with the actuator support structure and the top filter GAS blades resonances, respectively.

pendulum leg, gave the best results. The final result is shown in figure 5. The transfer function follows the $1/f^2$ slope up to about 20 Hz with an achieved isolation ratio below 2×10^{-4} from 20 Hz onwards.

In the earliest stages of the prototype tests [17], the performance of the inverted pendulum and the GAS filter chains have been characterized. The GAS blades are fabricated out of

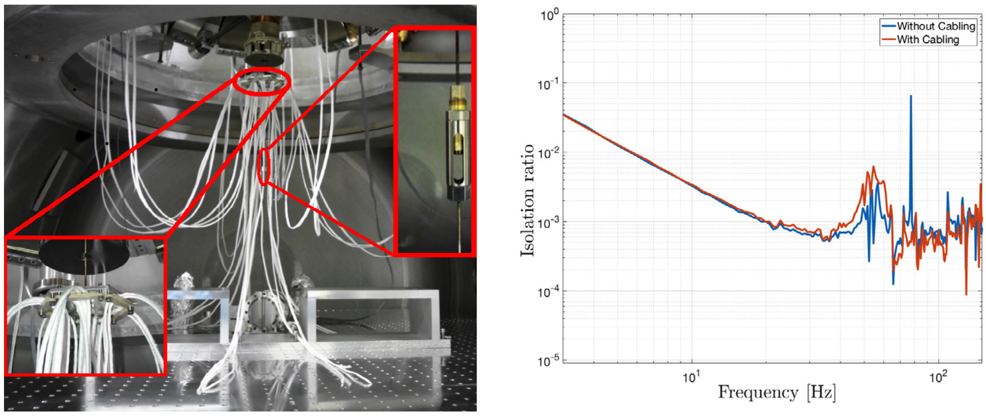

(a) (b)

Figure 8. Panel (a) shows a photograph of the area between intermediate filter to the bench. The right and left insets are zooms of the wire connector and the cable support plate, respectively. Panel (b) shows the horizontal transfer from intermediate filter to bench without and with cabling.

maraging steel, a low creep, high strength material [21, 22]. The transfer function from the base ring to the bench suspension point is obtained by combining the transfer functions of the inverted pendulum and the double pendulum. This results in the MultiSAS overall transfer function in horizontal. For vertical, a combination of the two GAS filters yields the overall transfer function. It features isolation ratios of 10^5 and 10^7 for vertical and horizontal motion, respectively, at 10 Hz as shown in figure 6.

The vertical and horizontal transfer function have a slope of $1/f^4$ and $1/f^6$, respectively, up to about 30 Hz. At the Virgo site, the typical seismic motion at 10 Hz is below 10^{-9} m $\mathrm{Hz}^{-1/2}$. The isolation performance of 10^7 in horizontal motion is sufficient by (more than) two orders of magnitude in order to meet the requirement of 2.1×10^{-12} m $\mathrm{Hz}^{-1/2}$ at 10 Hz.

The residual bench displacements and rotations due to ground rotation (yaw and tilt) are not deemed to be a problem. Firstly, the ground angular motion is typically below 1 nrad $\mathrm{Hz}^{-1/2}$ and, secondly, because the transfer to the bench above 10 Hz is small thanks to the thin wire suspension. The transfer function at 10 Hz is typically smaller than 10^{-7} for tilt-to-tilt and and 10^{-13} yaw-to-yaw. Therefore, the residual bench tilt and yaw at 10 Hz are below 10^{-16} rad $\mathrm{Hz}^{-1/2}$ and 10^{-22} rad $\mathrm{Hz}^{-1/2}$, respectively, both well below the requirement. Similarly, the tilt-to-horizontal displacement transfer (about 10^{-6} m rad^{-1} at 10 Hz) gives a residual bench displacement below 10^{-15} m $\mathrm{Hz}^{-1/2}$.

One other component of bench motion needs attention. It can be shown that the residual bench tilt θ_z due to horizontal ground motion can be related to the corresponding bench displacement x according to

$$I_{\mathrm{cm},z}\ddot{\theta}_z + m_{\mathrm{b}}h_{\mathrm{r}}\left(g\theta_z + \ddot{x}\right) = 0, \quad (1)$$

where $I_{\mathrm{cm},z}$ represents the moment of inertia around a (horizontal) axis and m_{b} the bench mass. The vertical distance between the bench CoM and the effective rotation point, $h_{\mathrm{r}} = h_{\mathrm{s}} + h_{\mathrm{b}}$, is the sum of the distance from the CoM to the wire suspension point h_{s} and the bending length $h_{\mathrm{b}} = \sqrt{EI/m_{\mathrm{b}}g}$, i.e. the distance from the wire suspension point to the effective rotation point. Here, EI represents the wire flexural rigidity. Equation (1) holds if the bending length is much smaller than the suspension wire length L_w, i.e. $h_b \ll L_w$. If also $|h_s| \ll L_w$, we are allowed to use the coupling between horizontal displacement and tilt which, by taking the Fourier transform of equation (1), is

$$\frac{\widetilde{\theta}_z}{\widetilde{X}} = \frac{\omega_{0,\theta_z}^2}{g} \frac{\omega^2}{\omega_{0,\theta_z}^2 - \omega^2}. \tag{2}$$

Here, $\omega_{0,\theta_z} = \sqrt{m_b g h_r / I_{cm,z}}$ denotes the bench tilt resonance frequency, which can be tuned arbitrarily low if needed by positioning the wire suspension point, if needed, below the bench center of mass ($h_s < 0$). For high frequencies ($\omega \gg \omega_{0,\theta_z}$), equation (2) reduces to

$$\frac{\widetilde{\theta}_z}{\widetilde{X}} = -\frac{\omega_{0,\theta_z}^2}{g}. \tag{3}$$

For the system considered here, the ratio h_r/L_w is typically below 1%, justifying the approximations leading to equations (1)–(3). As the tilt modes are typically not tuned below 150 mHz, this coupling can easily exceed 0.1 rad m^{-1}.

Such a large bench displacement-to-tilt coupling decreases the maximum allowed residual bench translation (table 1) by two orders of magnitude to about 10^{-14} m Hz$^{-1/2}$. In other words, the angular requirement of 3.3×10^{-15} rad Hz$^{-1/2}$ in combination with the coupling dictates the practical translational requirement. The translational requirement value listed before in table 1 resulted purely from the optical simulation which does not assume anything about the suspension system or its dynamics.

After MultiSAS was installed into a MiniTower further characterization was performed on the full mechanical assembly. Unwanted in-band (>10 Hz) resonances were identified by hammering tests, i.e. non-periodical hammering on strategic points of the mechanical structure and measuring the motion at strategic points using simple coil-magnet sensing. Additionally, transfer function measurements were performed and the system was studied with finite element modeling (FEM). Figures 7 and 8 show two important ones and our solutions to damp them.

The combined lateral and rotational modes of the keystone show up as large peaks in the transfer function. By placing a circular slab of steel on three pieces of viton on the keystone, its resonances are successfully damped, as shown in figure 7(b).

The bench is suspended from the intermediate filter by a two part wire with a steel connection joint, shown in figure 8(a). This joint is used to trim the vertical position of the bench. Its lateral *quasi violin modes* show up as a large peak at 75 Hz in the transfer function from the intermediate filter to the bench. Fortunately, electrical power and signal cables, carefully routed to the bench, via an aluminium support plate attached to the wire to maintain isolation performance, have a profound effect on this mode (see figure 8(b)). The mass of this holder is pushing the mode frequency down to about 55 Hz and helps to damp the peak.

4. Thermal shielding, acoustic coupling and leg parallelism measurement

Several aspects that could be detrimental to the seismic isolator performance have been characterized and mitigation strategies have been devised. Three of these possible issues, i.e. thermal effects on the GAS filters, acoustic couplings and the *cradle effect*, and their solution or mitigation are presented here.

In all Advanced Virgo suspended benches the front-end and digital processing electronics for the hosted photodetectors are housed in an air-tight container about 0.5 m^3 in volume which is a structural part of the bench itself. In this way, most of the otherwise needed cabling, that could act as a short for seismic noise, has been eliminated. All digital in/out signals are carried by highly mechanically compliant optical fibers, and the only cable routed throughout the bench suspension is the power supply one.

For maraging steel, the relative temperature dependence of the Young modulus $\gamma = (1/E)\mathrm{d}E/\mathrm{d}T = -230$ ppm K^{-1}, where γ represents the thermoelastic coefficient. Any temperature variation ΔT causes a change $\Delta F = \gamma \Delta T$ in load capacity, which amounts to -1.05 N K^{-1} and -0.78 N K^{-1} for the top and intermediate GAS filter, respectively. As a consequence of this thermo-elastic effect, the equilibrium positions of the filters drift by [23]

$$\Delta y_{\text{therm.el.}} = \frac{\Delta F}{k} = \frac{\gamma \Delta T}{m_{\text{load}} \omega_0^2}. \tag{4}$$

This results in a typical drift of 1.4 mm K^{-1} for a GAS filter tuned at 200 mHz. Strictly spoken the GAS spring stiffness k depends on the temperature as well. However, the effect on Δy is negligible, so it is not included in equation (4). Note that m_{load} is different for the two GAS filters; it is equal to the mass of the full chain for the top filter and to m_{b} for the intermediate filter.

In a GAS filter, a blade in the filter is bent and kept in this bent state by clamps which are bolted to the filter body, as visible in figure 2. The clamp exerts a horizontal compressive forces F_x on the blade. The thermal drift due to the differential thermal expansion coefficient between blade material and the filter body material is [23]

$$\Delta y_{\text{therm.exp.}} = \frac{F_x \Delta\alpha \Delta T}{L_{\text{bl}} m_{\text{load,bl}} \omega_0^2} (y - y_{\text{wp}}). \tag{5}$$

Here, L_{bl} represents the horizontal blade length, $m_{\text{load,bl}}$ the blade mass load, $\Delta\alpha$ the difference in thermal expansion coefficient, and y_{wp} the keystone nominal working point position, in which the vertical stiffness is minimum by definition. Note that Δy can be both positive and negative. The filter body material is stainless steel for both top and intermediate filters. The factor $(F_x \Delta\alpha)/(L_{\text{bl}} m_{\text{load,bl}} \omega_0^2)$ is $4.6 \times 10^{-4}\mathrm{K}^{-1}$ for typical values, so the thermal expansion contribution to Δy can be neglected when compared to the thermo-elastic effect.

A variation in temperature does not only cause a drift of the filter equilibrium position, but also slightly changes its working point resonance frequency. Contrary to the the thermal effects on equilibrium position, this is mainly due to the differential thermal expansion $\Delta\alpha$, and the resonance frequency changes as [23]

$$\frac{\Delta f}{\Delta T} \approx \frac{k_x \Delta\alpha}{2 m_{\text{load,bl}} f_0}, \tag{6}$$

where k_x represents the horizontal blade stiffness when it is bent. For a typical $m_{\text{load,bl}} = 40$ kg, $f_0 = 200$ mHz, $\Delta\alpha = 6 \times 10^{-6}\mathrm{K}^{-1}$ and $k_x = 110$ kN m^{-1} one may expect a resonance frequency temperature dependence of about 1 mHz K^{-1}. This estimation is valid provided the filter is controlled or retuned back to the working point.

Continuous compensation for the position drift Δy during operation of the sensing optics on the bench is provided by the top stage GAS filter built-in voice coil actuator. This actuator has a dynamic range of ± 1.5 N. Long term drift compensation can be made by using the fishing rod actuators installed on both the filters and with a dynamic range from 3.3 N to 9.3 N. MultiSAS can operate with a maximum thermal drift of ± 7.5 K from initial set point.

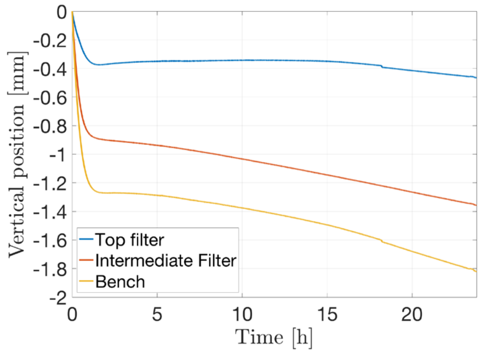

(a)

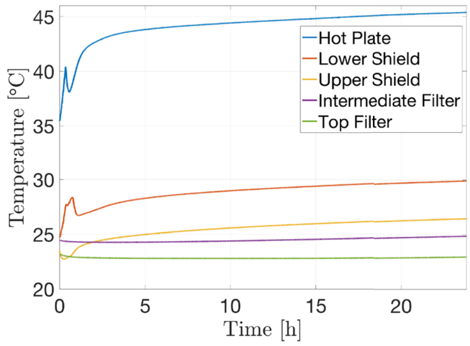

(b)

Figure 9. Thermal shield performance showing (a) the GAS filter keystone and bench position. The initial drop in the first hour is due to the air being pumped out. The small jump down around 18h into the test is attributed to hysterysis in the top stage blades. Panel (b) shows temperatures at several locations in the suspension chain during this measurement.

Since the benches are expected to operate in vacuum at a temperature around 40 °C, a thermal shield was designed and its efficiency tested on the MultiSAS prototype [24]. The thermal shield consists of a stack of two closely spaced (about 10 cm) non-anodized reflective aluminum sheets attached to the MultiSAS base ring. An anodized black aluminum *hot plate* to simulate the radiating surface of the warm optical bench equipped with resistive heaters was secured on top of the suspended bench.

In figure 9, results of a test are shown when both shields are reflective. The shields and the filter blades were significantly warmer when the temperature settled. The tests are performed as vacuum is achieved to simulate the particular situation after closing and pumping, as visible in figure 9(a) in the first hour. The buoyancy effect, because the bath of air in which the bench *floats* is slowly removed, increases the load for the MultiSAS and causes a sag of the bench. The load goes up by the volume of the bench and intermediate filter multiplied by the density of air and g.

The increasing temperature of the filter blades makes the keystones sag as visible in figure 9(a) after the first hour. Over a day the bench has sagged by almost 2 mm and longer tests have shown that this process continues. A simple exponential fit provides us with a time constant of 49.9 ± 0.9 h (95% confidence interval). The bench can end up 4 mm below its starting point, but this is within the range of the two fishing rods on the top and intermediate filter stage. In figure 9(b) we observe that, while the hot plate heats up to about 45 °C, the top stage and intermediate stage blades reach temperatures of 23 °C and 25 °C, respectively.

Operating a suspension in air has certain limitations at in-band ($f > 10$ Hz) frequencies. Acoustic pressure waves push on the otherwise isolated suspended object, such as an optical table. Removing the air eliminates the medium these pressure waves use to travel through and reduces the acoustic coupling. The acoustic coupling is expected to be negligible because the MiniTower will operate at a pressure below 10^{-5} mbar. This was tested to investigate how the bench ambient pressure relates to the acoustic coupling. Six inertial sensors, Sercel L22 geophones [25], were installed on the bench. With these six sensors (three horizontal and three vertical), the bench motion in all degrees of freedom can be reconstructed and the impact of acoustic noise can be evaluated. The limit of the measurement is set by the self noise of the

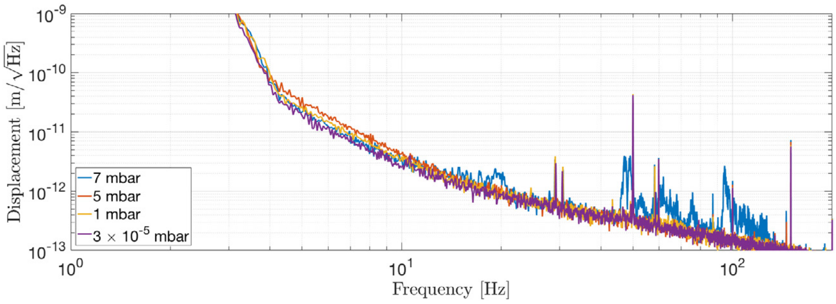

Figure 10. Acoustic coupling at a translationally and angularly controlled MultiSAS test facility suspended bench at different pressures for a horizontal L22 (out-of-loop) geophone on the bench. Clearly, the acoustic coupling falls below the L22 self noise below 5 mbar.

geophones. The self noise of the L22 geophone at 10 Hz is about 2×10^{-12} m $\text{Hz}^{-1/2}$ and falls of with $1/f$ from that point.

The horizontal coupling effect is displayed in figure 10. Below 5 mbar the acoustic coupling drops below the L22 self-noise. This indicates that, to maintain the translational isolation performance of MultiSAS, it must be operated at a pressure of 5 mbar or below. For the angular motion, for which a horizontal motion at the 10^{-15} m $\text{Hz}^{-1/2}$ is desirable, this measurement can give an upper limit.

Because of tolerances in machining and assembly, MultiSAS inverted pendulum legs will not be perfectly parallel and there might be a mismatch in leg length, causing similar effects as described below. In figure 11 a perfect stage is shown in the left picture, where lateral displacements do not result in the introduction of tilt to the top plate. The middle and right picture illustrate the possible non-parallel leg assembly. This is referred to as the *cradle effect*. Here, this effect is highly exaggerated, but two distinct cases can be distinguished when looking at the relative phase of the translation and tilt signals. The middle picture shows in-phase transfer from the x degree of freedom to θ_z, whereas the right picture shows a 180° out-of-phase transfer.

The parasitic coupling from displacement to tilt in the top stage must not exceed a certain value. This is because of the well known problem that inertial sensors (geophones in our case) are sensitive to both translation and tilt. The geophone signal of the top stage is not contaminated by tilt coupling down to $f_{\text{nt}} = 1/(2\pi)\sqrt{gc_{\text{hta}}}$, where c_{hta} is the coupling from a horizontal to an angular degree of freedom. This means, in order to have an inertial sensor correctly measuring the displacement down to frequencies were the sensor self-noise becomes dominant, i.e. 100 mHz, the coupling should not exceed the 4×10^{-2} rad m^{-1} level. Tests were performed on the MultiSAS prototype to measure the coupling coefficient, i.e. the misalignment between the inverted pendulum legs. An applied geomechanics 755-1129 Miniature Tilt Sensor was used to measure tilt. This sensor has a 100 nrad $\text{Hz}^{-1/2}$ resolution [26].

The measurement injected large 2 mm_{pp}, 5 mHz sinusoids in both horizontal x and z degrees of freedom. The injection is done at such a low frequency to be sure not to excite any modes of the suspension system, in particular the lowest resonance frequency modes. Table 2 shows the results of the two, several hour long injections, where immediately it can be seen that all couplings are below the 3×10^{-3} rad m^{-1} level. The results of the measurements show that the typical leg misalignment is on the safe side by more than one order of magnitude.

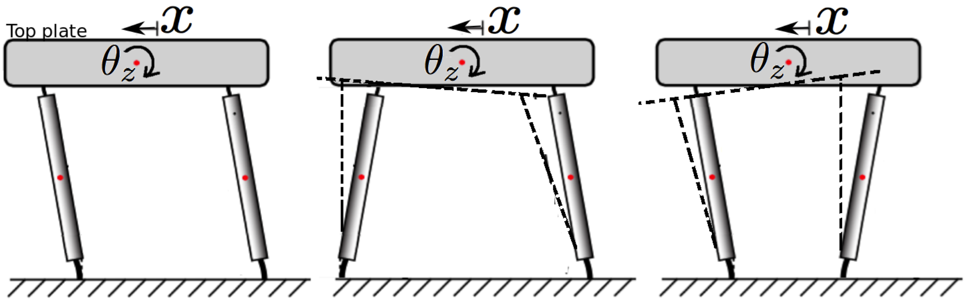

Figure 11. An overview of different possible cradle effects in the case of real world misalignments in leg-to-top-plate connections due to construction tolerances.

Table 2. Measured coupling factor c_{hta} and phase from horizontal to angular displacement for the top stage of the MultiSAS prototype. All couplings are more than one order of magnitude smaller than the maximum allowed value in order to have the geophones measure displacement instead of tilt down to 100 mHz.

	$x \to \theta_x$	$x \to \theta_z$	$z \to \theta_x$	$z \to \theta_z$	
c_{hta}	8×10^{-4}	1.5×10^{-3}	7×10^{-4}	2×10^{-3}	rad m^{-1}
Phase	180	0	0	0	deg

Measurements done on one of the MultiSASs for Advanced Virgo showed couplings all below the 3×10^{-3} rad m^{-1} level as well [27].

5. Control design and performance

To maintain MultiSAS at its operating point and provide optimal performance, active feedback is implemented. The error signals used for this control scheme are constructed from three LVDTs [20], three Sercel L4C geophones [25] placed on the top stage and, optionally, a tri-axial measurement of the ground motion. The LVDT is a differential DC sensor measuring the top stage position with respect to the reference frame which is connected to the MiniTower vacuum vessel. The L4C geophone is an inertial sensor. The signals from LVDTs and geophones are combined in the frequency domain (blended) to construct an inertial broadband super sensor with DC positioning. A cross-over frequency is about 160 mHz. Below this frequency, the LVDT signal is dominant and above it the geophone signal is dominant. Blending is done preferably below the microseismic peak, which is typically between 100–500 mHz [28], where it is desirable that the L4C inertial signal is dominant. The microseismic peak can then be suppressed better and the bench RMS motion can be reduced.

As the ground is in the LVDT signal with opposite sign, the ground measurement can be added to the LVDT signal. This process is called ground subtraction. At the prototype set-up, a Trillium T240 seismometer was used to measure the ground motion in three axes, i.e. the x-, y- and z-direction. Figure 12 shows the horizontal control strategy for MultiSAS in Virgo. The concept of blending or *sensor blending* or *sensor fusion* [29] was extensively used in the Virgo suspension control strategy [30]. Our control scheme features a fully digital control, using eight sensor inputs. These are blended to construct a DC coupled inertial signal for three horizontal degrees of freedom. Before blending, the signals are geometrically added using the

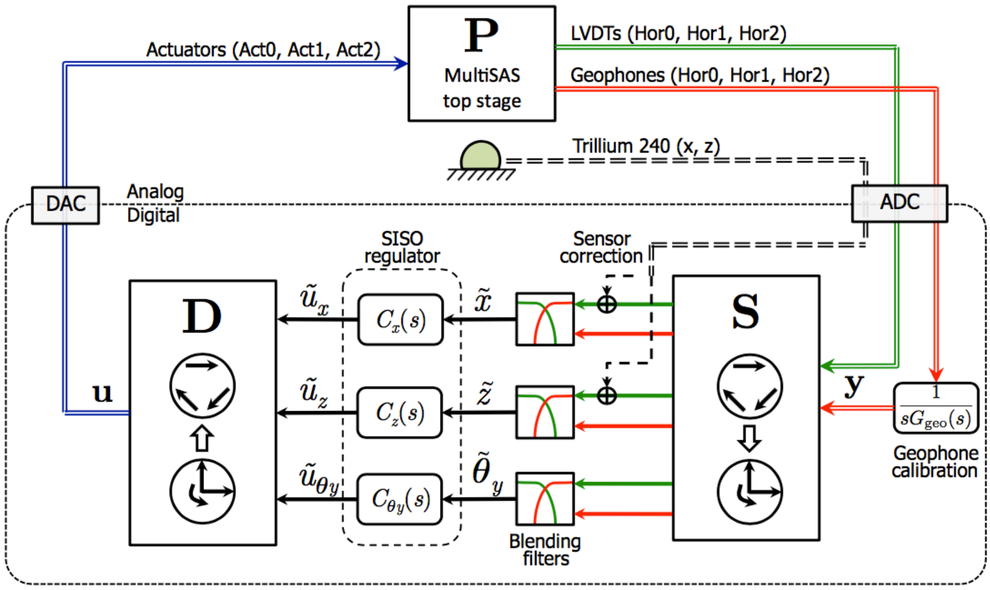

Figure 12. Digital control strategy for MultiSAS for degrees of freedom that are measurable with horizontal sensors at the top stage level. A multitude of sensor signals is geometrically added (using matrix S), blended to reconstruct virtual supersensors (x, z, θ_y) and implement single-input–single-output (SISO) control in those degrees of freedom. The orthogonal control signals are subsequently sent to each actuator using matrix D.

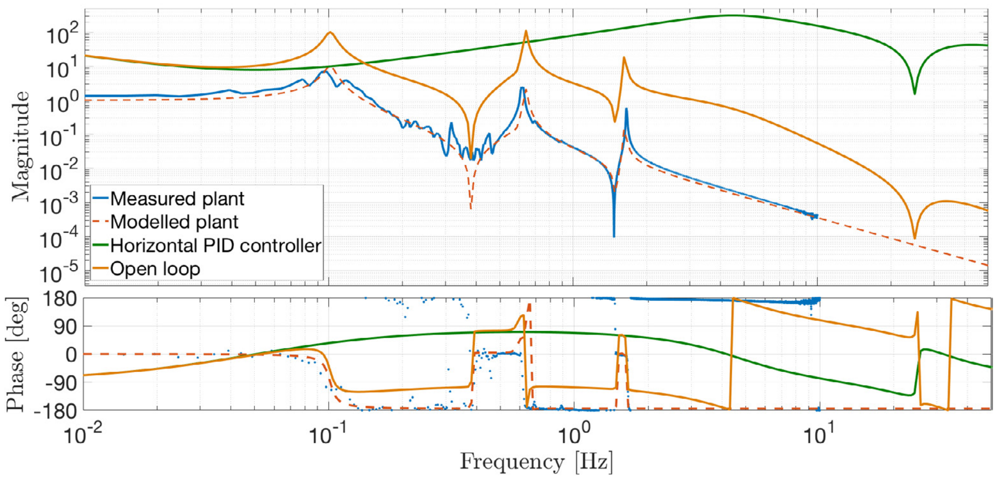

Figure 13. Loop transfer function design for the top stage MultiSAS horizontal degrees of freedom (x, z). A forced transfer function measurement of MultiSAS is compared to the modelled transfer function. The control filter is a conventional PID filter with a steep roll off provided by a 1st order elliptic filter with a notch at the MiniTower mode frequencies (here as an example at 25 Hz). Similar PID filters are used for the SISO regulators for θ_y and the y degree of freedom. All filters have a unity gain frequency at about 3 Hz and phase margins of more than 30°.

Table 3. Values for f and Q of the zeros and poles that make up the horizontal PID controller with elliptic roll-off filter. The real pole at 0 Hz represents the integrator. The other poles and zeros are complex or second order and the filter gain is about 90 at 1 Hz.

Zeros		Poles	
f (Hz)	Q	f (Hz)	Q
0.07	0.5	0	—
25	50	4.58	0.88
		30	0.5

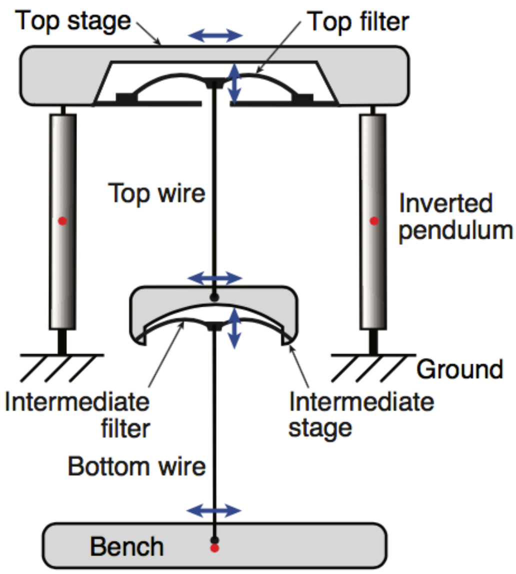

Figure 14. MultiSAS model showing the three horizontal and two vertical isolation stages. The ground is actually a support ring on top of the Minitower vacuum chamber, while the bench is simply sketched here as a thin plate.

sensing matrix **S**. This matrix is determined by the sensor geometrical location and is used to form an orthogonal set of the signals for x, z and θ_y).

The three horizontal error signals are sent to a SISO controller. As an example, the control loop design for x and z is shown in figure 13 with its zeros and poles presented in table 3. Visible in the plant transfer function are the main resonance modes of MultiSAS (blue and red curves in figure 13). The inverted pendulum stage has a resonance frequency of about 100 mHz. From the top stage the intermediate filter and suspended bench act as a double pendulum as discussed earlier. We can understand the transfer function using figure 14. The common pendulum mode in anti-phase with the top stage is located around 0.7 Hz. This mode in phase with the top stage generates the notch around 0.4 Hz. The differential pendulum mode, where the intermediate filter and bench (and top stage) move out of phase, is located around 1.8 Hz. The top stage and intermediate filter oscillating in phase result in the notch around 1.6 Hz.

The roll-off filter is a 1st order elliptic filter in combination with a 2nd order Butterworth filter at 30 Hz. The elliptic filter is used for a steep roll-off with minimal phase loss around the UGF. An additional benefit of the elliptic filter is that it features a notch, which can be aligned in frequency with the first rigid body mode of the MiniTower.

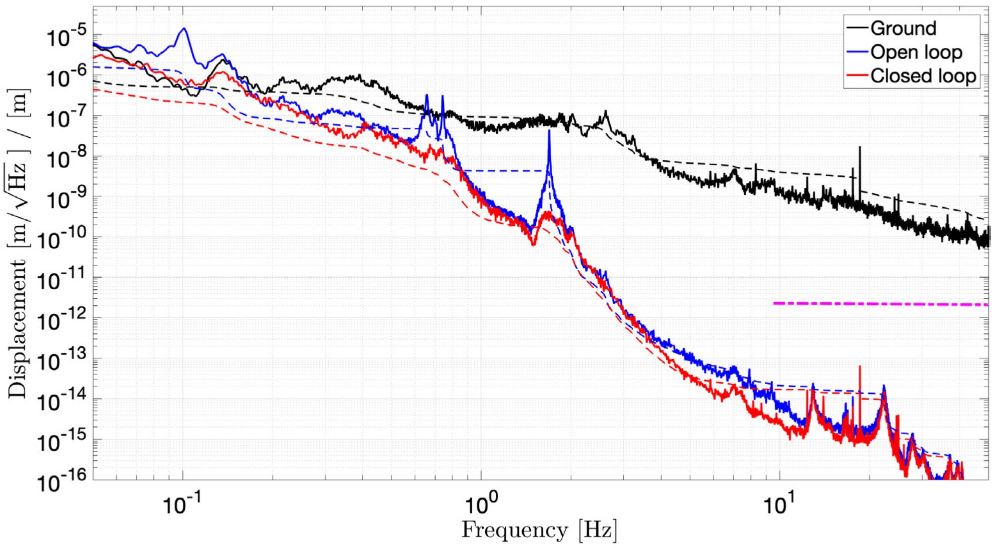

Figure 15. Projected open and closed loop spectral (solid) and RMS (dashed) bench motion in the z-direction. The microseismic peak between 100 and 500 mHz is clearly visible in the ground spectrum. The measurement is performed by a witness out-of-loop L4C geophone placed on the suspension top stage. Geophone high pass filters feature a cut-off at 50 mHz. The bench motion is projected by multiplying the witness sensor measurement with the top stage to bench transfer function, i.e. a (damped) double pendulum. The elevated spectra at frequencies below 100 mHz are attributed to ground tilt. The translational spectral requirement from 10 Hz is shown as a magenta dashed line. Displacement levels around or better than 10^{-14} m $\mathrm{Hz}^{-1/2}$ are achieved from 10 Hz onwards. At 12.8 and 22.3 Hz, the main modes of the MiniTower are observed.

MultiSAS was installed in the MiniTower and the bench was suspended from the lower wire. The actuation matrix **D** was determined first by using the iterative procedure described in [17], and then the operation in closed-loop was tested. Typical results are shown in figure 15. The microseismic peak provides the largest contribution to the integrated motion of the ground [28]. At 10 Hz, the ground motion is below 10^{-8} m $\mathrm{Hz}^{-1/2}$ and at higher frequencies the usual $1/f^2$ slope is observed.

An out-of-loop witness geophone was placed on the top stage in order to measure the system performance. The signal of the witness geophone was also used to estimate the residual motion of the suspended bench. This is achieved by multiplying the witness sensor signal by the measured and subsequently modelled top stage to bench transfer function. It must be noted that this projection gives a more realistic estimate of the residual bench motion since, unlike the MultiSAS transfer function of figure 6, it also includes the mechanical response of the Minitower to the ground motion.

In open loop, the MultiSAS modes at around 0.1 Hz, 0.7 Hz and 1.8 Hz are observed. The attenuation slope increases to $1/f^6$ above the last mode at 1.8 Hz. The translational ASD requirement is surpassed by more than two orders of magnitude in the horizontal degree of freedom. When the rigid body modes of the suspension are effectively damped by the controls, the integrated RMS displacement reduces to a fraction of a micron.

The MiniTower vacuum vessel modes must be monitored as this motion couples to angular motion. In figure 15, the tank modes are clearly visible in the top stage motion and can end up as horizontal motion at the suspended bench level. This motion couples directly to pitch and

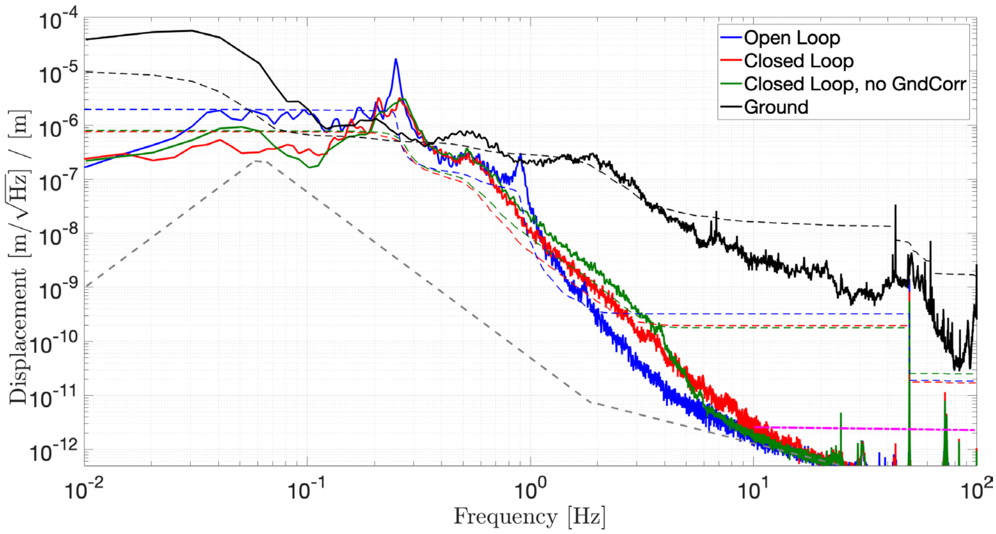

Figure 16. Measured open and closed loop spectral (solid) and RMS (dashed) results, with and without ground correction, in the vertical y-direction reconstructed by three Sercel L22 geophones. The dashed grey line represents the L22 geophone noise model [25] with high-pass filters around 50 mHz to avoid unbounded integration at DC. Both the closed loop traces RMS meet the micron requirement, but there is some injection between 0.8 and 8 Hz for the uncorrected case. All L22 traces hit the sensor self-noise just below 10 Hz. The translational spectral requirement from 10 Hz is shown as a magenta dashed line. The elevated ground spectrum at frequencies below 100 mHz is attributed to ground tilt.

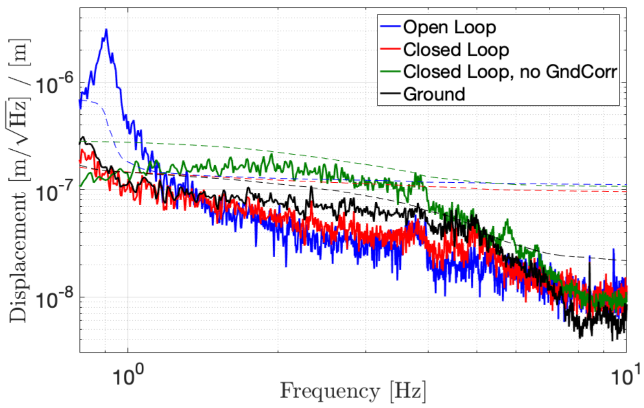

Figure 17. Open and closed loop spectral (solid) and RMS (dashed) results in the y-direction measured by the in-loop ($\leqslant$4 Hz) LVDT with and without ground correction.

roll and could spoil the angular performance as described in section 3. As there are no commercial sensors available to measure down to this level, a test was made with a custom made inertial sensor with interferometric readout [31, 32]. Bench motion of 8×10^{-15} m Hz$^{-1/2}$ from 30 Hz onwards was measured limited by the sensor self-noise. Continued development to reach the modelled sensor self-noise of 3×10^{-15} m Hz$^{-1/2}$ from 10 Hz is ongoing.

The use of low frequency blending makes the ground subtraction in horizontal less crucial. However, the vertical motion is only sensed by a single LVDT bolted to the keystone of the top GAS filter. Ground motion subtraction is vital for this degree of freedom. A similar PID filter as presented in figure 13 and table 3 is used. Results of control performance are visible in figure 16. The vertical signal shown is a reconstruction of three vertical L22 geophones located 120° apart on an imaginary 1 m diameter circle on the bench. The common and differential GAS modes are visible around 0.25 and 0.9 Hz, respectively. Both closed loop spectra show injection between 1 and 6 Hz. This is attributed to gain peaking of the loop and can possibly be resolved by improved loop design. The elevated closed loop spectrum without ground subtraction is observed in figure 17. Although the vertical top stage LVDT is an in-loop sensor up until about 4 Hz, this result corroborates the vertical L22 results.

In the Advanced Virgo systems, the GAS filters are tuned to lower frequency (0.2 Hz individually) and these modes are found at around 0.2 and 0.6 Hz. The use of a geophone for control of the vertical degree of freedom was considered, but not deemed necessary to meet requirements and difficult due to space constraints in the current MultiSAS design. Advanced control strategy experiments [33] have made use of a geophone on the payload.

6. Conclusions and future work

The measurement of GWs has been possible because critical optical elements of the detectors have been seismically decoupled from the Earth's ever-present seismic motion. In the Advanced Virgo design, the decoupling is necessary for the core optics of the detector as well as the auxiliary optics. Some of these auxiliary optics are housed on optical benches, which are decoupled using vibration isolation systems. Five MultiSAS have been designed to isolate optical benches, but the design can be suitably adapted to suspend any kind of (optical) element needing the typical seismic isolation required in gravitational wave interferometers.

FEM and state space modelling were used to identify the (internal) mechanical modes of the system, and vibration dampers were designed and installed where necessary. In the first characterization campaign the systems behaved according to expectation, and met the Advanced Virgo design requirements.

Thermal shielding is a specific feature designed for GAS filters and was tested to ensure that the sagging of the GAS filter blades did not extend beyond the reach of the fishing rod. MultiSAS operates as expected and meets all of the current requirements. Tests have shown that a pressure of 1 mbar is sufficient to reduce acoustic coupling to below measurable levels. The construction tolerances are such that the cradle effect impacts on the inertial sensor performance on the top stage used for control.

If tilt motion is to be decreased further, one solution would be to lower the frequency of the suspended bench angular modes (now around 300 mHz for all suspended benches) to below 100 mHz by lowering the suspension point more towards the bench center of mass. Lowering these mode frequencies will also prevent alignment with the microseismic peak.

The KAGRA detector has adopted similar designs for the vibration isolation of its core optics. Systems inspired by the MultiSAS design are planned to suspend the squeezing optical table and (filtering) cavity mirrors for Advanced Virgo. The Australian National University (ANU) Centre for Gravitational Physics will use MultiSAS to suspend their low-frequency torsional pendulum TorPeDO [34]. The test facility now serves as ultra-quiet platform for development of advanced seismic sensors [35, 36] and as a controls test-bed.

Further advancement in control strategies, such as was already done for the vertical degree of freedom with a dummy mass as suspended load [33], will improve both translational and angular RMS performance by better predicting the plant behavior upon actuation and using that information accordingly. The future systems can be used for (auxiliary) optics suspensions for future GW detectors, such as Einstein telescope [37] or Cosmic explorer [38].

Acknowledgments

The authors would like to thank R Mittleman and E Majorana for their extensive review of this paper. We would also like to thank Michiel Jaspers, Willem Kuilman and Arnold Rietmeijer for constructing the MultiSAS prototype set-up and their hands-on experience in improving the design for the five Advanced Virgo systems. A thank you to Marco Kraan for producing the artist impressions of the system is in order as well. Lastly, Fred Schimmel has designed our Labview measurement tools. This work is (partly) financed by the Netherlands Organisation for Scientific Research (NWO).

ORCID iDs

J V van Heijningen https://orcid.org/0000-0002-8391-7513

References

[1] Abbott B P *et al* 2016 Observation of gravitational waves from a binary black hole merger *Phys. Rev. Lett.* **116** 061102
[2] Acernese F *et al* 2014 Advanced Virgo: a second-generation interferometric gravitational wave detector *Class. Quantum Grav.* **32** 024001
[3] Aasi J *et al* 2015 Advanced LIGO *Class. Quantum Grav.* **32** 074001
[4] Abbott B P *et al* 2017 GW170814: a three-detector observation of gravitational waves from a binary black hole coalescence *Phys. Rev. Lett.* **119** 141101
[5] Abbott B P *et al* 2017 GW170817: observation of gravitational waves from a binary neutron star inspiral *Phys. Rev. Lett.* **119** 161101
[6] Abbott B P *et al* 2017 Multi-messenger observations of a binary neutron star merger *Astrophys. J. Lett.* **484** L12
[7] Accadia T *et al* 2011 Performance of the Virgo interferometer longitudinal control system during the second science run *Astropart. Phys.* **34** 521–7
[8] Ballardin G *et al* 2001 Measurement of the VIRGO superattenuator performance for seismic noise suppression *Rev. Sci. Instrum.* **72** 3643
[9] Accadia T *et al* 2010 Noise from scattered light in Virgo's second science run data *Class. Quantum Grav.* **27** 194011
[10] Ottaway D J, Fritschel P and Waldman S J 2012 Impact of upconverted scattered light on advanced interferometric gravitational wave detectors *Opt. Express* **20** 8329–36
[11] Lück H *et al* 2008 Opto-mechanical frequency shifting of scattered light *J. Opt. A: Pure Appl. Opt.* **10** 085004
[12] Mantovani M 2012 SBE suspension requirements for automatic alignment purposes *Technical Report EGO* VIR-0101A-12
[13] Bertolini A *et al* 2001 Recent progress on the R&D program of the seismic attenuation system (SAS) proposed for the advanced gravitational wave detector, LIGO II *Nucl. Instrum. Methods Phys. Res.* A **461** 300–3
[14] Stochino A *et al* 2009 The seismic attenuation system (SAS) for the Advanced LIGO gravitational wave interferometric detectors *Nucl. Instrum. Methods Phys. Res.* A **598** 737–53
[15] Wanner A *et al* 2012 Seismic attenuation system for the AEI 10 m prototype *Class. Quantum Grav.* **29** 245007
[16] Marka S *et al* 2002 Anatomy of TAMA SAS seismic attenuation system *Class. Quantum Grav.* **19** 1605–14

[17] Beker M G 2013 Low-frequency sensitivity of next generation gravitational wave detectors *PhD Thesis VU* University Amsterdam
[18] Cella G *et al* 2005 Monolithic geometric anti-spring blades *Nucl. Instrum. Methods Phys. Res.* A **540** 502–19
[19] Akutsu T *et al* 2018 Construction of KAGRA: an underground gravitational wave observatory *Prog. Theor. Exp. Phys.* **2018** 013F01
[20] Tariq H *et al* 2002 The linear variable differential transformer (LVDT) position sensor for gravitational wave interferometer low-frequency controls *Nucl. Instrum. Methods Phys. Res.* A **489** 570–6
[21] Braccini S *et al* 2000 The maraging-steel blades of the Virgo super attenuator *Meas. Sci. Technol.* **11.5** 467
[22] Virdone N *et al* 2008 Extended-time-scale creep measurement on Maraging cantilever blade springs *Nucl. Instrum. Methods Phys. Res.* A **593** 597–607
[23] Blom M R 2015 Design and performance of the external injection bench seismic attenuation system EIB-SAS *PhD Thesis VU* University Amsterdam
[24] Bertolini A *et al* 2014 MultiSAS heat shielding test results *Technical Report* Virgo note VIR-0497A-14
[25] Kirchhoff R *et al* 2017 Huddle test measurement of a near Johnson noise limited geophone *Rev. Sci. Instrum.* **88** 115008
[26] Applied Geomechanics 756-series mid-range Miniature Tilt sensors (www.tech-sys.be/pdf/755-75620l00007d.pdf) (Accessed: 1 November 2014)
[27] van Heijningen J V 2018 Low-frequency performance improvement of seismic attenuation systems and vibration sensors for next generation gravitational wave detectors *PhD Thesis VU* University Amsterdam
[28] Peterson J 1993 *Observations and Modeling of Seismic Background Noise* (U.S. Department of Interior Geological Survey) (https://doi.org/10.3133/ofr93322)
[29] Matichard F *et al* 2015 Seismic isolation of Advanced LIGO: review of strategy, instrumentation and performance *Class. Quantum Grav.* **32** 185003
[30] Losurdo G *et al* 2006 The control of the Virgo superattenuator revised (I). Inertial damping: present and future *Technical Report* Virgo note VIR-NOT-FIR-1390-318
[31] van Heijningen J V *et al* 2016 Interferometric readout of a monolithic accelerometer, towards the fm $\sqrt{\mathrm{Hz}}^{-1}$ resolution *Nucl. Instrum. Methods Phys. Res.* A **824** 665–9
[32] van Heijningen J V *et al* 2018 A novel interferometrically read out inertial sensor for future gravitational wave detectors *IEEE SAS Proc.* pp 76–80
[33] Beker M G *et al* 2014 State observers and kalman filtering for high performance vibration isolation systems *Rev. Sci. Instrum.* **85** 034501
[34] McManus D J *et al* 2017 Mechanical characterisation of the TorPeDO: a low frequency gravitational force sensor *Class. Quantum Grav.* **34** 135002
[35] Boom B A *et al* 2017 Nano-g accelerometer using geometric anti-springs *IEEE 30th Int. Conf. on MEMS Proc.* pp 33–6
[36] Beker M *et al* 2016 Innovations in seismic sensors driven by the search for gravitational waves *Leading Edge* **35** 590–3
[37] Abernathy M *et al* 2011 Einstein gravitational wave telescope conceptual design study *Technical Report* ET-0106C-10 (www.et-gw.eu/index.php/etdsdocument)
[38] Abbot B P *et al* 2017 Exploring the sensitivity of next generation gravitational wave detectors *Class. Quantum Grav.* **34** 044001